Eur. Phys. J. D **11**, 45–58 (2000)

THE EUROPEAN
PHYSICAL JOURNAL D
EDP Sciences

Proton and electron impact on molecular and atomic oxygen: II. Emission cross-sections for ionisation and excitation of atomic oxygen

O. Wilhelmi and K.-H. Schartner[a]

I. Physikalisches Institut, Justus-Liebig-Universität, 35392 Giessen, Germany

Received 9 September 1999 and Received in final form 15 December 1999

Abstract. Ionisation and excitation of atomic oxygen in collisions with protons and electrons were studied experimentally in the intermediate velocity range applying the method of fluorescence spectroscopy. Absolute emission cross-sections for $2s$-electron ionisation, excited ion production and excitation of atomic oxygen are presented and for electron impact compared to available data. For proton impact no emission cross-sections have been published so far.

PACS. 34. Atomic and molecular collision processes and interactions –
32.70.-n Intensities and shape of atomic spectral lines

1 Introduction

Ionisation and excitation processes of atomic oxygen are of strong interest in astrophysics, ionospheric and atmospheric physics or plasma diagnostics. Although electrons, protons or photons impinge on atomic oxygen quite frequently in natural environments and artificial plasmas, experimentalists still face difficulties in providing an atomic oxygen target for their studies and only limited experimental data exist. Fluorescence spectroscopy enables remote investigation of excited oxygen atoms and ions, but absolute emission cross-sections are required as input for calculations and in order to interpret fluorescence spectra.

Furthermore, ionisation and excitation of atomic oxygen offer the opportunity to examine structure and dynamics of an open shell system. In contrast to the easily available rare gases, angular momentum coupling results in three states of the ground state $2p^4$ electron configuration. Theoretical treatment of atomic oxygen as well as experiments put an ambitious task to the scientist.

Though a number of approaches to determine VUV emission cross-sections resulting from electron impact on atomic oxygen have been carried out [1–6], experimental difficulties led to large uncertainties and to deviations between the different results. We present the so far most comprehensive compilation of experimental absolute emission cross-sections in the VUV spectral range for electron and proton impact on O, all measured with the same experimental setup, supplying best comparability for both projectiles and all investigated transitions. For proton impact no experimental partial cross-sections have so far been available. Electrons and protons in the intermediate velocity range were employed (electron energies: 200 eV–2 keV, proton energies: 17 keV–800 keV). The intermediate velocity range links the description of the collision by the first Born approximation as high velocity limit with the quasimolecular low velocity limit.

Absolute emission cross-sections for electron and proton impact on O_2 and highly resolved fluorescence spectra are presented in the preceding paper I [7]. The experimental setup for the present study has also been used for measuring photoionisation of O [8]. Photodissociation of O_2 into neutral fragments has been investigated in a related project [9].

2 Experimental

2.1 Investigated processes

The ionisation and excitation processes with the subsequent radiative decay of the excited ions or atoms for which absolute emission cross-sections are presented, are summarized in this section. The excited electron, the produced vacancy or the open shell electrons label the atomic and ionic states.

$$\begin{gathered}2s^{-1}\text{ ionisation:}\\ e^-,\ p^+ + \mathrm{O}\ (2p^4\ {}^3\mathrm{P}^e)\\ \downarrow\\ e^-,\ p^+ + \mathrm{O}^+\ (2s^{-1}\ {}^4\mathrm{P}^e,\ {}^2\mathrm{D}^e,\ {}^2\mathrm{S}^e,\ {}^2\mathrm{P}^e) + e^-\\ \downarrow\\ \mathrm{O}^+\ (2p^3\ {}^4\mathrm{S}^o,\ {}^2\mathrm{D}^o,\ {}^2\mathrm{P}^o) + h\nu_{\mathrm{fl}},\end{gathered}\tag{1}$$

---

[a] e-mail:
`karl-heinz.schartner@exp1.physik.uni-giessen.de`

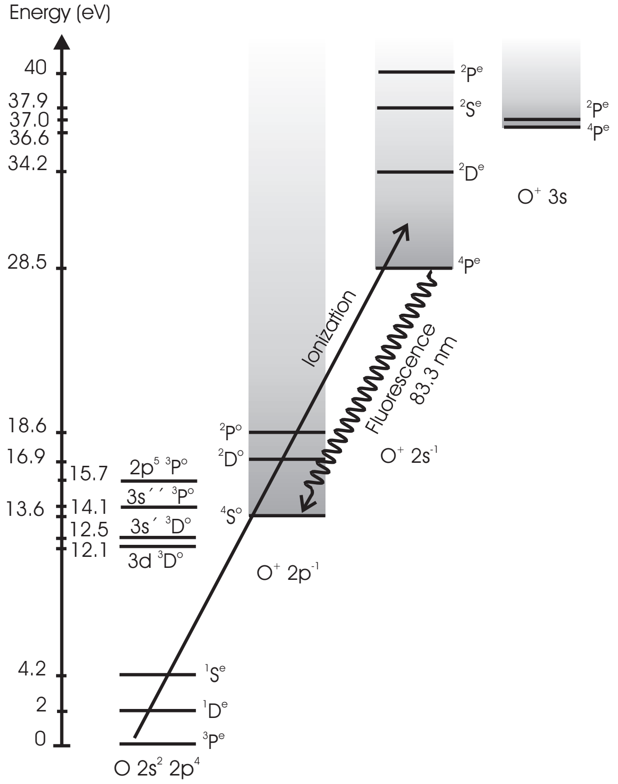

Fig. 1. Atomic energy levels and single ionisation thresholds and continua for all states discussed in this work. One example for $2s^{-1}$ ionisation into O^+ ($2s^{-1}$ $^4\mathrm{P}^e$) followed by the radiative $2p \rightarrow 2s$ transition is illustrated by the arrows.

ion excitation:

$$
\begin{gathered}
e^-,\ p^+ + \mathrm{O}\ (2p^4\ {}^3\mathrm{P}^e) \\
\downarrow \\
e^-,\ p^+ + \mathrm{O}^+\ (3s\ {}^4\mathrm{P}^e,\ {}^2\mathrm{P}^e) + e^- \\
\downarrow \\
\mathrm{O}^+\ (2p^3\ {}^4\mathrm{S}^o,\ {}^2\mathrm{D}^o,\ {}^2\mathrm{P}^o) + h\nu_{\mathrm{fl}},
\end{gathered}
\tag{2}
$$

excitation:

$$
\begin{gathered}
e^-,\ p^+ + \mathrm{O}\ (2p^4\ {}^3\mathrm{P}^e) \\
\downarrow \\
e^-,\ p^+ + \mathrm{O}\ (3d\ {}^3\mathrm{D}^o,\ 3s'\ {}^3\mathrm{D}^o,\ 3s''\ {}^3\mathrm{P}^o,\ 2p^5\ {}^3\mathrm{P}^o) + e^- \\
\downarrow \\
\mathrm{O}^+(2p^4\ {}^3\mathrm{P}^e) + h\nu_{\mathrm{fl}}.
\end{gathered}
\tag{3}
$$

The wavelengths of the fluorescence photons, indicated by $h\nu_{\mathrm{fl}}$ in equations (1–3), and the respective fluorescent transitions are listed in Table 1. Figure 1 shows the energy levels of equations (1–3) with one example for a $2s$-electron ionisation followed by radiative decay of the ionic state.

Table 1. Fluorescence wavelengths and electronic transitions for the absolute emission cross-sections determined in this study.

Fluorescence wavelength	Electronic transition
	$2s$-electron ionisation
83.3 nm	O^+: $2s2p^4\ {}^4\mathrm{P}^e \rightarrow 2s^22p^3\ {}^4\mathrm{S}^o$
58.1 nm	O^+: $2s2p^4\ {}^2\mathrm{P}^e \rightarrow 2s^22p^3\ {}^2\mathrm{P}^o$
53.8 nm	O^+: $2s2p^4\ {}^2\mathrm{P}^e \rightarrow 2s^22p^3\ {}^2\mathrm{D}^o$
71.9 nm	O^+: $2s2p^4\ {}^2\mathrm{D}^e \rightarrow 2s^22p^3\ {}^2\mathrm{D}^o$
79.7 nm	O^+: $2s2p^4\ {}^2\mathrm{D}^e \rightarrow 2s^22p^3\ {}^2\mathrm{P}^o$
64.4 nm	O^+: $2s2p^4\ {}^2\mathrm{S}^e \rightarrow 2s^22p^3\ {}^2\mathrm{P}^o$
	ion excitation
53.9 nm	O^+: $2s^22p^2({}^3\mathrm{P}^e)3s\ {}^4\mathrm{P}^e \rightarrow 2s^22p^3\ {}^4\mathrm{S}^o$
61.7 nm	O^+: $2s^22p^2({}^3\mathrm{P}^e)3s\ {}^2\mathrm{P}^e \rightarrow 2s^22p^3\ {}^2\mathrm{D}^o$
67.3 nm	O^+: $2s^22p^2({}^3\mathrm{P}^e)3s\ {}^2\mathrm{P}^e \rightarrow 2s^22p^3\ {}^2\mathrm{P}^o$
	excitation
79.2 nm	O: $2s2p^5\ {}^3\mathrm{P}^o \rightarrow 2s^22p^4\ {}^3\mathrm{P}^e$
87.9 nm	O: $2s^22p^3({}^2\mathrm{P}^o)3s\ {}^3\mathrm{P}^o \rightarrow 2s^22p^4\ {}^3\mathrm{P}^e$
98.9 nm	O: $2s^22p^3({}^2\mathrm{D}^o)3s\ {}^3\mathrm{D}^o \rightarrow 2s^22p^4\ {}^3\mathrm{P}^e$
102.7 nm	O: $2s^22p^3({}^4\mathrm{S}^o)3d\ {}^3\mathrm{D}^o \rightarrow 2s^22p^4\ {}^3\mathrm{P}^e$

2.2 Experimental setup

A microwave driven atomic oxygen discharge source was set up at a 1 MeV van de Graaff accelerator for the proton impact measurements. An electron gun could be mounted alternatively. Partially dissociated oxygen was emerging from the source in an effusive beam, which was intersected by the projectile beam. Fluorescence emitted in transitions from excited ionic and atomic states was dispersed in the VUV spectral region by a 1-m normal-incidence monochromator. A two-dimensional position sensitive detector, mounted in the position of the exit slit, allowed to register fluorescence from different transitions simultaneously. Normalisation to absolute emission cross-sections was carried out by comparison with reference emission cross-sections in argon and krypton. Fluorescence in the visible and near UV spectral region was dispersed by a second monochromator and recorded in order to support the analysis of the effusive beam.

2.3 Atomic oxygen source – setup

The atomic oxygen source consists of a pyrex discharge tube inserted into a rectangular microwave hollow guide as sketched in Figure 2. Microwaves at 2.45 GHz with 120 W power propagate in the hollow guide terminated by a movable short circuit. Incident and reflected waves interfere to yield a standing wave pattern. By adjusting the short circuit, an electric field maximum forms in the discharge tube. Impedance matching is achieved with

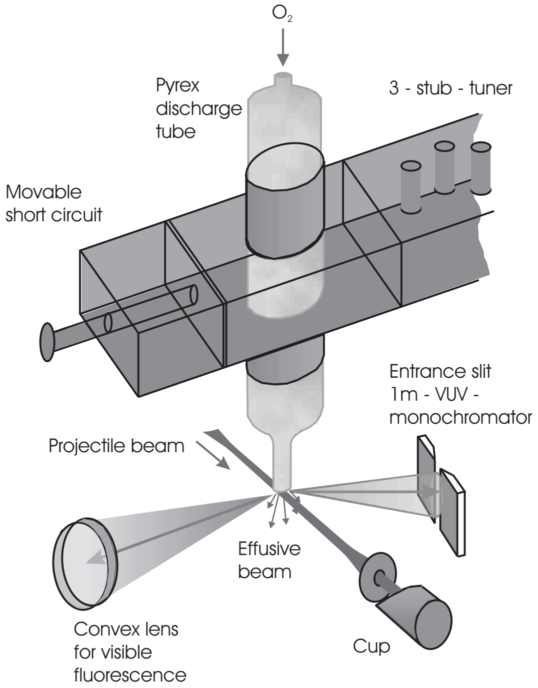

Fig. 2. Overview of the atomic oxygen source.

a 3-stub-tuner. Two microwave chimneys, enclosing the discharge tube and acting as mismatched hollow guides, avoid microwave power to be radiated out of the hollow guide. Discharge ignition has to be enforced by a high voltage spark.

The discharge volume is 18 mm in diameter and is limited in its downstream extension by a 6 mm aperture separating the discharge volume from a 95 mm long exit channel. At the end of the exit channel, a teflon nozzle (0.8 mm in diameter, 3 mm long) forms the effusive beam and maintains the pressure difference between discharge tube and interaction region. At a constant mass flow of 1 sccm O_2 fed to the discharge tube, the source pressure is estimated to be 0.8 mbar, causing a background pressure of approximately 1×10^{-4} mbar. In order to improve stability of the discharge and to increase the dissociation fraction, a small amount of methane CH_4 (3–5%) is added to the mass flow. The discharge tube is manufactured with a surrounding cooler and can thus be cooled by a flow of cold nitrogen vapour, produced by electric heating of liquid nitrogen in a closed dewar container. No coating or surface treatment was applied to the pyrex discharge tube.

2.4 The 1 MeV van de Graaff accelerator and the electron gun

Projectile beams intersected the effusive beam 3 mm below nozzle exit. The intersection position was defined by five aligned circular apertures, the smallest one 2.5 mm in diameter. The apertures served as a differential pumping stage to keep the vacuum in the accelerator beamline and at the electron gun on a suitable level. In order to monitor the position of the projectile beam, the apertures were electrically insulated and the projectile current on the apertures was measured. The projectile beam current passing through all apertures was collected in a cup. The 1 MeV van de Graaff accelerator focussed a proton beam with energies from 90 keV to 800 keV and typical currents between 15 μA and 20 μA through the experimental arrangement. At proton energies below 70 keV the proton currents were limited to 2–4 μA due to the focusing properties of the ion lenses. Electron beams with energies between 200 eV and 2 keV were provided by a modified TV electron gun. Careful screening of magnetic stray fields was carried out. Since the projectile current was used to normalise the fluorescence signal, all measured currents in the cup and on the apertures behind the effusive beam were summed. The apertures were set to potentials of +40 V to correct the measured currents for secondary electrons.

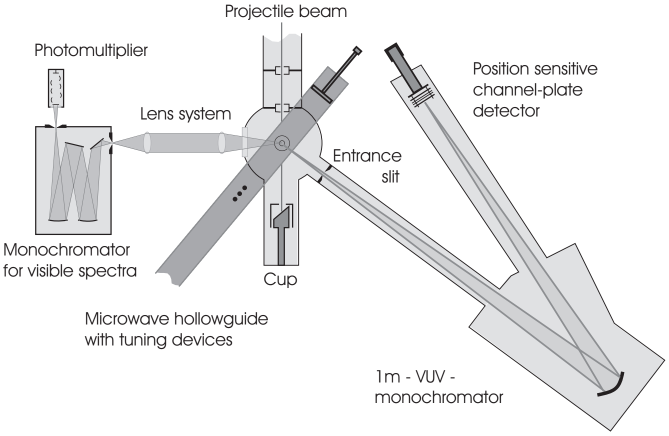

Fig. 3. Top-view of the experimental setup, illustrating the detection branches for VUV and visible/near UV fluorescence.

2.5 Fluorescence detection in the VUV spectral region

The VUV fluorescence from radiative transitions of excited O^+ and O states was dispersed by a 1-m normal-incidence monochromator, mounted under the magic angle with respect to the projectile beam (Fig. 3). The magic angle mount suppressed the influence of the angular distribution of the detected fluorescence intensities. The monochromator was equipped with a 1200 lines per mm, osmium coated grating blazed at 60 nm. A fluorescence wavelength range from 40 nm to 125 nm was observed. The entrance slit of the 1-m normal-incidence monochromator was set to 200 μm.

A two dimensional position sensitive multichannel-plate detector allowed to detect a spectral range of 35 nm simultaneously, thus requiring measurements at three grating positions to cover the wavelength range of interest. Figure 4 displays spectra recorded for 2 keV electron impact with discharge on and off.

The relative spectral quantum efficiency was obtained from fluorescence line intensity measurements on Ar and

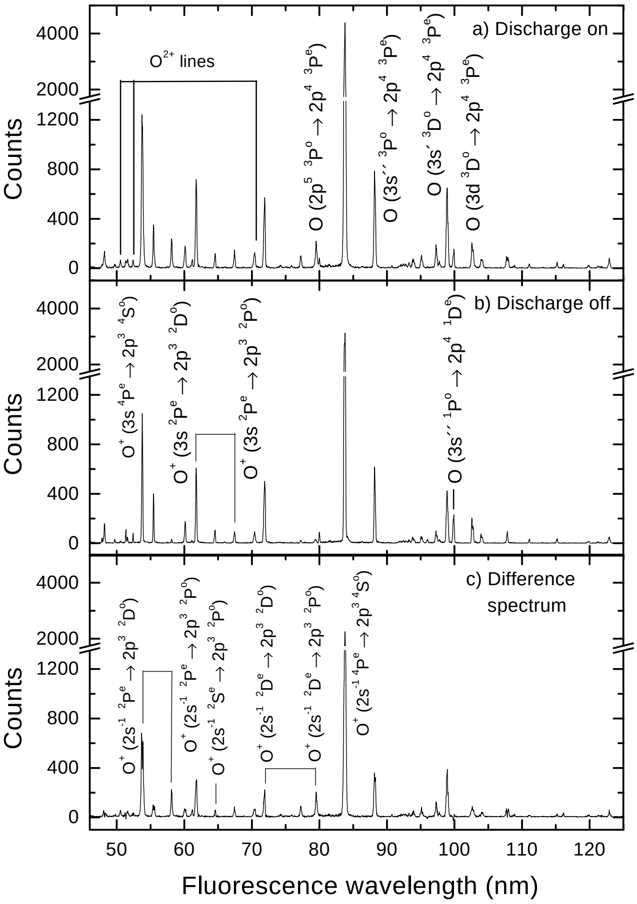

Fig. 4. VUV spectra resulting from 2 keV electron impact on effusive beams: top graph – discharge on, center graph – discharge off. The bottom graph shows the difference spectrum derived according to equation (6) from the spectra with discharge on and off. Spectra are not corrected for spectral quantum efficiency of the present grating-detector combination.

Kr effusive beams under 2 keV electron impact. Fluorescence intensity ratios were compared to accurate emission cross-sections ratios by Jans *et al.* [10]. The determination of the spectral quantum efficiency was restricted to a wavelength interval between 54.32 nm and 96.50 nm. Due to the weak reflectivity of the grating above 100 nm fluorescence wavelength, no quantitative analysis of fluorescence lines with wavelengths longer than that of the 102.7 nm line could be carried out.

The influence of resonance radiation trapping has been tested by reducing the mass flow which has shown to be in good approximation equivalent to reducing the target density. Figure 5 illustrates the mass flow dependence of the intensities of two fluorescence lines resulting from excited O states. The linear relation between the experimental intensities and the mass flow allows to exclude resonance radiation trapping, considering the relative low density and the localized target volume.

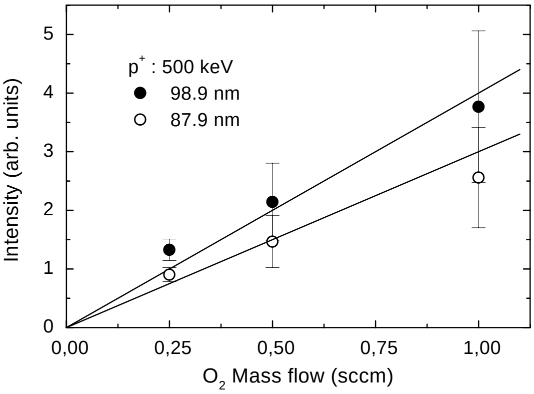

Fig. 5. The dependence of fluorescence intensity on mass flow (target density) for the fluorescence lines at 87.9 nm and 98.9 nm resulting from excitation of O ($2p^4$ ^{3}P^o) into O ($3s''$ ^{3}P^o) and O ($3s'$ ^{3}D^o).

2.6 Fluorescence detection in the visible/near UV spectral region

Simultaneously to VUV fluorescence detection, fluorescence in the near UV/visible spectral range of 260–670 nm from ionisation and excitation of O and O_2 was recorded to support the effusive beam analysis. A telescopic mounting of two lenses was used in order to match the solid angle of a Czerny-Turner type monochromator (Fig. 3). The monochromator was equipped with a 1200 lines per mm grating. No position sensitive detection device was available in this case, so a Peltier cooled photomultiplier was used. All window and lens material was quartz to allow for fluorescence detection of the 2nd negative band system of O_2^+ at wavelengths down to 280 nm. A step motor, turning the grating in order to scan the wavelength, was controlled by a projectile current integrator. Fluorescence intensities registered for all wavelengths were thus normalised to projectile flux. Because of the low intensity and in order to cover the complete wavelength range from 260–670 nm within the time disposable for the experiments, a slit width of 1 mm had to be chosen. The identification of emission features is based on high resolution spectra for 2 keV electron impact on O_2 presented in paper I [7].

The teflon nozzle of the discharge tube was wrapped with aluminium foil not only to avoid upcharging, but also to screen light from the discharge. Straylight spectra yielded low intensities which were nevertheless subtracted from the impact induced spectra with discharge on.

2.7 Effusive beam analysis

Fluorescence originating from excited O^+ or O states either resulting from projectile impact on O or from impact dissociation of O_2 had to be separated. For that purpose the composition of the effusive beam had to be determined.

2.7.1 Dissociation fraction

The most important parameter describing the composition of the effusive beam is the degree of dissociation D, *i.e.* the ratio of dissociated molecules to the molecules fed to the discharge. The degree of dissociation was extracted from the fluorescence of the transition O $(3s''\ ^1\mathrm{P}^o) \rightarrow$ O $(2p^4\ ^1\mathrm{D}^e)$ at 99.9 nm with discharge on and off. The short interaction time of the fast projectile electrons prevents electron exchange and leads to target spin conservation in electron collisions. In case of proton impact the interaction of projectile and target does also not affect the spin. Therefore singlet states can not be excited from the atomic oxygen triplet ground state and fluorescence from the above singlet transition results from dissociative excitation of molecules. With the discharge on, a decrease of this fluorescence intensity is observed, which indicates a decrease of molecules in the effusive beam due to dissociation. The relative loss of intensity from dissociative excitation gives the relative loss of molecules in the effusive beam. The degree of dissociation D therefore follows from the intensity ratio of the line at 99.9 nm with discharge on and off:

$$D = 1 - \frac{I_{\text{discharge on}}(99.9\ \text{nm})}{I_{\text{discharge off}}(99.9\ \text{nm})}\,. \qquad (4)$$

The degree of dissociation was averaged over the measurements at each projectile energy:

$$D = 0.22 \pm 0.024$$

i.e. 22% of the O_2 molecules are lost by dissociation. At a mass flow of 1 sccm O_2 fed to the discharge, the effusive beam contains a massflow of 2×0.22 sccm $= 0.44$ sccm atoms. An average density of oxygen atoms in the interaction region of 1.5×10^{13} cm^{-3} is estimated. This value was derived from an effusive beam simulation (*cf.* Sect. 2.8.1).

The degree of dissociation was measured alternatively by comparing the intensities of the first negative band system of O_2^+ $(b\ ^4\Sigma_g^- \rightarrow a\ ^4\Pi_u)$ with the discharge on and off. Since dissociation in the discharge reduces the density of molecules in the effusive beam, a proportional decrease in intensity of the molecular band emission is observed:

$$D = 1 - \frac{\sum\limits_{\Delta\nu} I_{\text{discharge on}}(b\ ^4\Sigma_g^- \rightarrow a\ ^4\Pi_u)}{\sum\limits_{\Delta\nu} I_{\text{discharge off}}(b\ ^4\Sigma_g^- \rightarrow a\ ^4\Pi_u)}\,. \qquad (5)$$

The average degree of dissociation obtained from equation (5) is

$$D = 0.24 \pm 0.032.$$

D was measured at each projectile energy and the fluorescence intensity resulting from projectile impact on the molecules in the effusive beam was subtracted to get the fluorescence intensities originating from ionisation and excitation of atomic oxygen only (Fig. 4):

$$I_{\text{atom}} = I_{\text{discharge on}} - (1-D) I_{\text{discharge off}}\,. \qquad (6)$$

2.7.2 Test of metastable atoms

As can be seen in Figure 1, two metastable atomic states O $(2p^4\ ^1\mathrm{D}^e)$ and O $(2p^4\ ^1\mathrm{S}^e)$ of the ground state configuration exist. The appearance of metastable atoms in the effusive beam was probed in a separate photoionisation experiment at the synchrotron radiation facility BESSY using the present experimental setup [8]. The fluorescence intensity from the transition O^+ $(2s^{-1}\ ^2\mathrm{D}^e) \rightarrow$ O^+ $(2p^3\ ^2\mathrm{D}^o)$ at 71.9 nm was registered while scanning the exciting photon energy from 28 eV to 42 eV in steps of 100 meV. A threshold energy of 32.2 eV is necessary for $2s^{-1}$ ionisation of O $(2p^4\ ^1\mathrm{D}^e)$ into O^+ $(2s^{-1}\ ^2\mathrm{D}^e)$. At 32.2 eV no threshold behaviour was observed, instead a threshold for fluorescence emission was found at 34.2 eV, the threshold energy for $2s^{-1}$ ionisation of O $(2p^4\ ^3\mathrm{P}^e)$ into O^+ $(2s^{-1}\ ^2\mathrm{D}^e)$. The fluorescence from O^+ $(2s^{-1}\ ^2\mathrm{S}^e)$ at 64.4 nm increased at the O $(2p^4\ ^3\mathrm{P}^e) \rightarrow \mathrm{O}^+$ $(2s^{-1}\ ^2\mathrm{S}^e) + e^-$ threshold and not at the O $(2p^4\ ^1\mathrm{S}^e) \rightarrow \mathrm{O}^+$ $(2s^{-1}\ ^2\mathrm{S}^e) + e^-$ threshold.

Since $2s^{-1}$ photoionisation channels without recoupling of the angular momenta of the $2p$-electrons are favoured ($\Delta L = 0$), but the less preferred ionisation channels which imply angular momentum recoupling are observed, we exclude the survival of metastable atoms from the discharge in the effusive beam. For a detailed discussion we refer to our paper on photoionisation of O [8].

2.7.3 Test of metastable molecules

Although no metastable atoms were found in the effusive beam, metastable molecules might still be present. The relevant molecular states are O_2 $(a\ ^1\Delta_g)$ and O_2 $(b\ ^1\Sigma_g^+)$. Metastable molecular states are not only produced in the discharge, but can also result from recombination of O in wall collisions in exit channel and nozzle. In order to test the presence of metastables in the effusive beam, especially of the longer-living O_2 $(a\ ^1\Delta_g)$, fluorescence from the first and second negative band system of O_2^+ was measured. Spectra recorded for projectile impact on the effusive beam with discharge on show fluorescence emission in the second negative band system of O_2^+ whereas this emission features can hardly be distinguished from noise in the spectra from an effusive beam with discharge off (Fig. 6). The fluorescence of the second negative band system of O_2^+ in the difference spectrum in Figure 6 (bottom) is attributed to ionisation of the metastable O_2 $(a\ ^1\Delta_g)$.

In consequence, the influence of metastable molecules in the O_2 $(a\ ^1\Delta_g)$ state on the determination of the degree of dissociation in equations (4, 5) has to be discussed. The fluorescence intensity emitted in the first negative band system of O_2^+ results from ionisation of the triplet ground state O_2 $(X\ ^3\Sigma_g^-)$, since the the molecular quartet state O_2^+ $(b\ ^4\Sigma_g^-)$ of the first negative band system of O_2^+ cannot be excited from the metastable singlet state O_2 $(a\ ^1\Delta_g)$ due to spin conservation in the ionisation process. Therefore the degree of dissociation derived from the

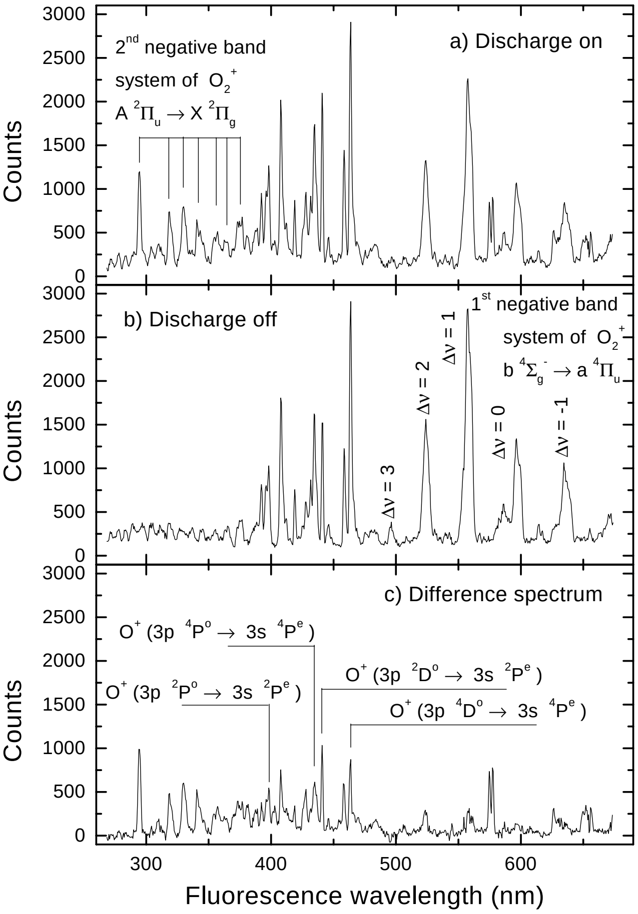

Fig. 6. Visible and near UV spectra resulting from 200 keV proton impact on effusive beams: top graph – discharge on, center graph – discharge off. The bottom graph shows the difference spectrum derived according to equation (6) from the spectra with discharge on and off. Spectra are not corrected for spectral quantum efficiency of the detection system.

intensity ratio of the first negative band system of O_2^+ with discharge on and off (Eq. (5)) reflects the total loss of O_2 $(X\ ^3\Sigma_g^-)$ in the effusive beam, including the conversion to metastable states.

In order to estimate the effect of metastable molecules in the O_2 $(a\ ^1\Delta_g)$ state on the degree of dissociation derived from equation (4), we assume that the unknown 99.9 nm line emission cross-section resulting from dissociative excitation of O_2 $(a\ ^1\Delta_g)$ into O $(3s''\ ^1P^o)$ fragments is in the same order of magnitude as the 99.9 nm line emission cross-section resulting from dissociative excitation of O_2 $(X\ ^3\Sigma_g^-)$ into O $(3s''\ ^1P^o)$ fragments. Then the degree of dissociation gives the decrease of molecules independent of their electronic state and a O_2 $(a\ ^1\Delta_g)$ molecule is treated in the same way as a O_2 $(X\ ^3\Sigma_g^-)$ molecule. Following this argumentation, the difference of 0.02 between the degrees of dissociation from both methods is due to an approximate mass flow of 0.02×1 sccm = 0.02 sccm of O_2 $(a\ ^1\Delta_g)$ in the effusive beam.

We draw the conclusion that only a few percent of the target density consist of metastable molecules in the O_2 $(a\ ^1\Delta_g)$ state.

2.7.4 Test of ions

In the atomic VUV spectra in Figure 4 appear three isolated, weak fluorescence lines of O^{2+} at 50.8 nm, 52.5 nm and 70.3 nm, all emitted by O^{2+} states of the $2s2p^3$ configuration. Assuming the $2s^{-1}$ ionisation cross-section of O $(2p^4)$ to be in the same order of magnitude as the $2s^{-1}$ ionisation cross-section of O^+ $(2p^3)$, an estimation of ions in the effusive beam becomes feasible. The intensity ratio of fluorescence resulting from $2s^{-1}$ ionisation of O^+ to fluorescence resulting from $2s^{-1}$ ionisation of O, *e.g.* $I(70.3\ \text{nm})/I(83.3\ \text{nm}) = 0.015$, reflects the upper limit of the relative contribution of ions to the effusive beam. Since O^{2+} states can also be populated by double ionisation of O, it seems reasonable to assume that ions are neutralized in wall collisions.

2.7.5 Composition of the effusive beam

The spectroscopic analysis of the effusive beam from a discharge fed with 1 sccm O_2 leads to the result that it mainly consists of 0.76 sccm ground state molecules O_2 $(X\ ^3\Sigma_g^-)$ and 0.44 sccm ground state atoms O $(2p^4\ ^3P^e)$. Only a small contribution of metastable molecules O_2 $(a\ ^1\Delta_g)$ was found. This result agrees with investigations of effusive beams of similar atomic oxygen sources [19–25].

2.8 Normalisation procedure

Absolute emission cross-sections have been obtained by normalising the intensities of the VUV emission lines to fluorescence lines with known emission cross-section, resulting from Ar 3*s*-electron ionisation by 2 keV electrons [10] or 300 keV and 800 keV protons [29], in both cases under the same experimental conditions. The fluorescence wavelengths of the subsequent Ar^+ $3p \rightarrow 3s$ transitions are 93.2 nm and 92.0 nm. The target density effects were investigated in a simulation of the effusive beam.

2.8.1 Simulation of the effusive beam

The described normalisation procedure requires information about at least the relative O and Ar target densities in the interaction region. Under molecular flow conditions equal mass flows of O and Ar yield target densities that differ due to the different atomic weight. The cooling of the discharge tube leads to the same mean kinetic energies for O from the discharge and for Ar. Therefore the ratio of the mean particle density was expected to equal $\sqrt{m_{\mathrm{Ar}}/m_{\mathrm{O}}} = 1.58$.

In a refined consideration, a simulation of the density profiles in the effusive beam [27] was carried out, based on an effusive beam description by Pauly [26]. The simulation takes collisions in the nozzle into consideration and assumes molecular flow in the effusive beam itself (opaque mode). Simulating effusive beams for different mass flows led to target densities proportional to mass flow. This result agrees with the observed fluorescence intensity dependence on mass flow in Figure 5. Integrating the simulated density distribution over the interaction region leads for equal mass flows to a factor 1.37 rather than 1.58 for the Ar to O density ratio. The factor 1.37 is taken into account in the normalisation of fluorescence intensities to absolute emission cross-sections.

2.9 Experimental uncertainties

Statistical errors of the emission cross-sections result from the standard deviations of the intensity signals $I_{\text{discharge on}}$, $I_{\text{discharge off}}$ and the degree of dissociation D contributing to equation (6). In the mean the statistical errors amount to 15%.

Additionally, systematic errors due to the normalisation of registered fluorescence intensities to absolute emission cross-sections have to be taken into account. For the reference cross-section taken from the electron collision experiment performed by Jans *et al.* [10] an error of 2.8% is reported. Absolute cross-sections taken from the proton collision experiment of Hippler and Schartner [29] have an error of 25%. The systematic error of the relative quantum efficiency correction was determined to be 23%. The difference of the degree of dissociation derived from VUV spectra and visible spectra was taken as systematic error of the degree of dissociation; it amounts to 9%. A systematic error in target density caused by a possible variation in the intersection of projectile beam with the O/O_2 effusive beam on the one hand and with the Ar or Kr effusive beams on the other hand was deduced from different simulated overlaps, resulting in 22%. The sum of the relative systematic errors yields 57% for electron impact emission cross-sections and 79% for proton impact emission cross-sections. The respective root sum square uncertainties are 33% and 41%.

3 Results and discussion

3.1 Emission cross-sections for transitions in O^+ resulting from $2s^{-1}$ ionisation of O

Ionisation of a $2s$-electron of O ($2p^4\ {}^3\mathrm{P}^e$) leads to one of four final ionic states: O^+ ($2s^{-1}\ {}^4\mathrm{P}^e$), O^+ ($2s^{-1}\ {}^2\mathrm{D}^e$), O^+ ($2s^{-1}\ {}^2\mathrm{S}^e$) or O^+ ($2s^{-1}\ {}^2\mathrm{P}^e$). One of the $2p$-electrons of these ionic states relaxes to fill the vacant $2s$-hole state *via* a radiative transition. The various transitions with the respective fluorescence wavelengths are listed in Table 1. The energies of the O^+ ($2s^{-1}$) states (Fig. 1) prevent autoionisation (O^{2+} states energies $\geq$ 48.736 eV [11]), so there are no non-radiative decay channels. Kelly [11] specified one cascade transition O^+ ($2s\,2p^3\,3s\ {}^4\mathrm{S}^o$) $\rightarrow$ O^+ ($2s^{-1}\ {}^4\mathrm{P}^e$) at 74.0 nm. Since the intensity at 74.0 nm is extremely weak (Fig. 4), we consider cascade population as negligible in case of the O^+ ($2s^{-1}$) states. For that reasons, the sum of the emission cross-sections of fluorescence lines emitted from one O^+ ($2s^{-1}$) state equals the corresponding $2s^{-1}$ partial ionisation cross-section.

- O^+ ($2s^{-1}\ {}^4\mathrm{P}^e$) and O^+ ($2s^{-1}\ {}^2\mathrm{P}^e$)

The 83.3 nm line emission cross-sections resulting from ionisation into O^+ ($2s^{-1}\ {}^4\mathrm{P}^e$) and the 58.1 nm line and 53.8 nm line emission cross-sections resulting from ionisation into O^+ ($2s^{-1}\ {}^2\mathrm{P}^e$) are presented in Figure 7 along with the experimental 83.3 nm line emission cross-sections of Zipf *et al.* [2] for electron impact and with theoretical electron and proton impact ionisation cross-sections of Peach [15]. Line graphs are fitted to our emission cross-sections in order to guide the eye. The employed fitting functions are discussed in Section 3.4. The fluorescence emission at 53.8 nm from O^+ ($2s^{-1}\ {}^2\mathrm{P}^e$) cannot be resolved from fluorescence emission at 53.9 nm from O^+ ($3s\ {}^4\mathrm{P}^e$). To obtain the plotted emission cross-sections for the 53.8 nm line, the line graphs fitted to the emission cross-sections for the 58.1 nm line were multiplied by the intensity branching ratio 4.0, measured in [14].

The 83.3 nm line emission cross-sections for electron impact on O determined by Zipf *et al.* [2] are a factor 3 larger than the present experimental data. We note here that the 83.3 nm line emission cross-sections for electron impact on O_2 given by Zipf *et al.* [2] in the same publication are a factor 2 smaller than the emission cross-sections from our experimental study of electron and proton impact on O_2 in paper I [7]. The 83.3 nm line emission cross-section ratio resulting from ionisation of O to dissociative ionisation of O_2 both into O^+ ($2s^{-1}\ {}^4\mathrm{P}^e$) is a factor 6 smaller than that of Zipf *et al.* [2]. The large difference in this cross-section ratio is not understood, especially since it cannot stem from the systematic uncertainty of the absolute emission cross-sections.

The theoretical O^+ ($2s^{-1}\ {}^4\mathrm{P}^e$) ionisation cross-sections for proton and electron impact of Peach [15] exceed our 83.3 nm line emission cross-sections at specific projectile energies above 100 keV/amu approximately by a factor 6. We state that the theoretical $2s^{-1}$ ionisation cross-sections for Ne in the same paper of Peach [15] were found to overestimate the corresponding emission cross-sections measured by our group with a different experimental arrangement [28] likewise by a factor 6. In the bottom graph of Figure 7 it is seen, that the theoretical O^+ ($2s^{-1}\ {}^2\mathrm{P}^e$) ionisation cross-sections of Peach [15] exceed the sum of the 53.8 nm line plus 58.1 nm line emission cross-sections. The top graph of Figure 7 illustrates the sum of the O^+ ($2s^{-1}\ {}^4\mathrm{P}^e$) plus O^+ ($2s^{-1}\ {}^2\mathrm{P}^e$) ionisation cross-sections for electron impact from a theoretical calculation by Chung *et al.* [16]. The theoretical ionisation cross-section of Chung *et al.* [16] at 200 eV electron energy is 13.8 Mb, the sum of our experimental 83.3 nm line plus 53.8 nm line plus 58.1 nm line emission cross-sections for 200 eV electron impact yields 9.5 Mb.

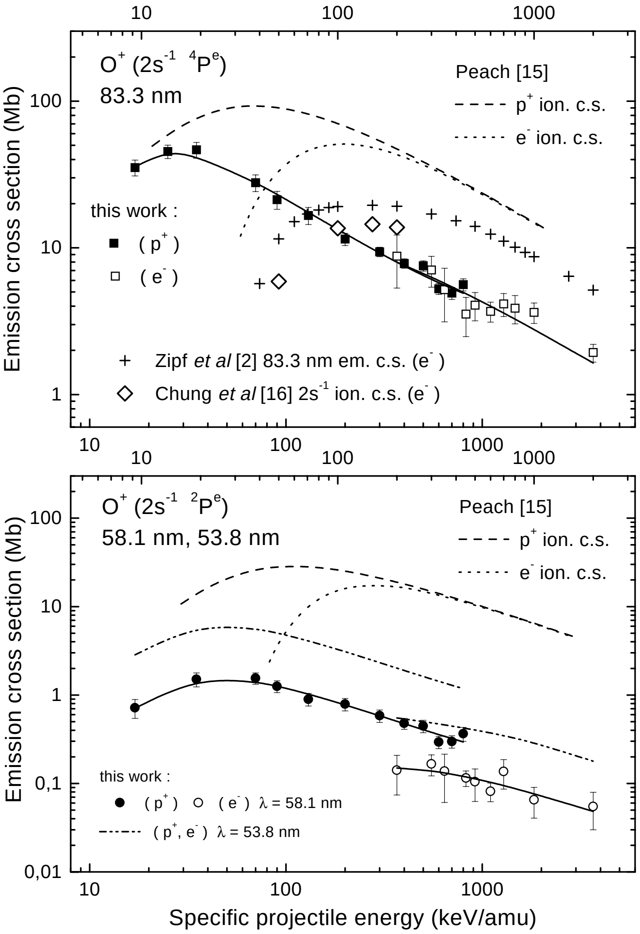

Fig. 7. Emission cross-sections for fluorescence lines resulting from $2s^{-1}$ ionisation into the O^+ ($2s^{-1}$ $^4P^e$) and O^+ ($2s^{-1}$ $^2P^e$) states by proton impact (compact symbols) and electron impact (open symbols) as function of specific projectile energy (proportional to the square of the projectile velocity). The fitting functions are plotted as line graphs. Error bars include statistical errors only. The 53.8 nm line emission cross-section function is calculated from the 58.1 nm line results using the 53.8 nm line/58.1 nm line branching ratio 4.0 [14]. The dashed/dotted curves represent O^+ ($2s^{-1}$ $^4P^e$) ionisation cross-sections for proton/electron impact calculated by Peach [15], the crosses experimental 83.3 nm line emission cross-sections determined by Zipf *et al.* [2]. Theoretical O^+ ($2s^{-1}$ $^4P^e$) plus O^+ ($2s^{-1}$ $^2P^e$) ionisation cross-sections of Chung *et al.* [16] are shown as open diamonds (top).

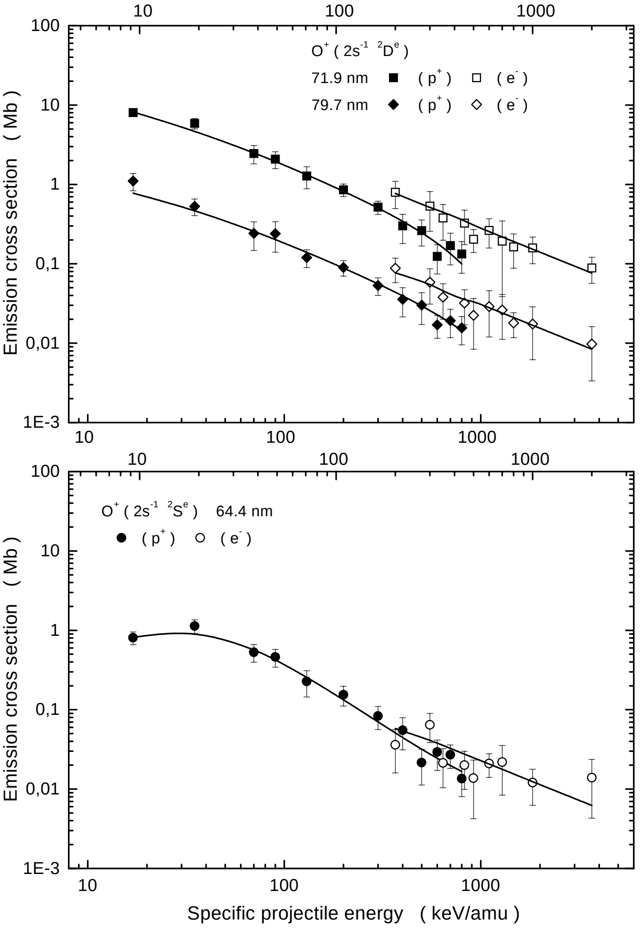

Fig. 8. Emission cross-sections for fluorescence lines resulting from $2s^{-1}$ ionisation into the O^+ ($2s^{-1}$ $^2D^e$) and O^+ ($2s^{-1}$ $^2S^e$) states by proton impact (compact symbols) and electron impact (open symbols) as function of specific projectile energy (proportional to the square of the projectile velocity). The fitting functions are plotted as line graphs. Error bars include statistical errors only.

- O^+ ($2s^{-1}$ $^2D^e$) and O^+ ($2s^{-1}$ $^2S^e$)

Figure 8 shows the emission cross-sections of the fluorescence lines 71.9 nm and 79.7 nm, subsequent to $2s^{-1}$ ionisation into the O^+ ($2s^{-1}$ $^2D^e$) state and of the fluorescence line at 64.4 nm resulting from $2s^{-1}$ ionisation into the O^+ ($2s^{-1}$ $^2S^e$) state. Neither theoretical nor experimental studies have considered these ionisation channels before. Both differ substantially from $2s^{-1}$ ionisation into the ionic states O^+ ($2s^{-1}$ $^4P^e$) and O^+ ($2s^{-1}$ $^2P^e$), because ionisation can no longer be regarded as merely ejecting a $2s$-electron. Since the $2s$-electron has no angular momentum before ionisation, its removal should not affect the total angular momentum, *i.e.* $2s^{-1}$ ionisation of the O ($2p^4$ $^3P^e$) ground state should lead to O^+ ($2s^{-1}$ $^4P^e$) and O^+ ($2s^{-1}$ $^2P^e$) only. The observed $2s^{-1}$ ionisation into O^+ ($2s^{-1}$ $^2D^e$) and O^+ ($2s^{-1}$ $^2S^e$) prove the necessity of a more elaborate consideration of the dynamics of the ionisation process or the structure of atomic and ionic states. Evidence for ionisation into the O^+ ($2s^{-1}$ $^2D^e$) and O^+ ($2s^{-1}$ $^2S^e$) states was also found in our photoionisation experiment, supported by theoretical photoionisation cross-sections of McLaughlin [8]. The theoretical results were obtained by employing multi-configuration interaction wavefunctions based on 15 O^+ states in LS-coupling. Hints on successive collisions of the projectile with two target electrons or a collision of the ejected electron with a bound electron are discussed in Section 3.4.

For the intensity ratio of the 79.7 nm line to the 71.9 nm line emitted from O^+ ($2s^{-1}$ $^2D^e$), an average value of 0.109 ± 0.014 was obtained for proton impact

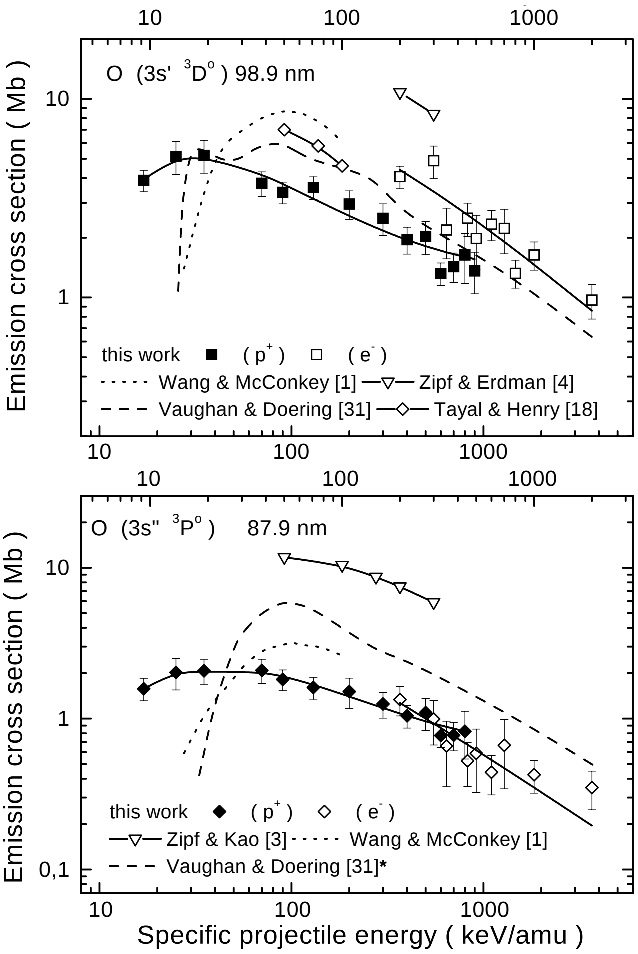

Fig. 9. Emission cross-sections for fluorescence lines resulting from excitation into the O ($3s'$ ^{3}D^o) and O ($3s''$ ^{3}P^o) states by proton impact (compact symbols) and electron impact (open symbols) as function of specific projectile energy (proportional to the square of the projectile velocity). The fitting functions are plotted as line graphs. Error bars include statistical errors only. Our results are compared to published data from various experimental and theoretical investigations. $*$ indicates conversion of excitation cross-sections into emission cross-sections applying the autoionisation factors.

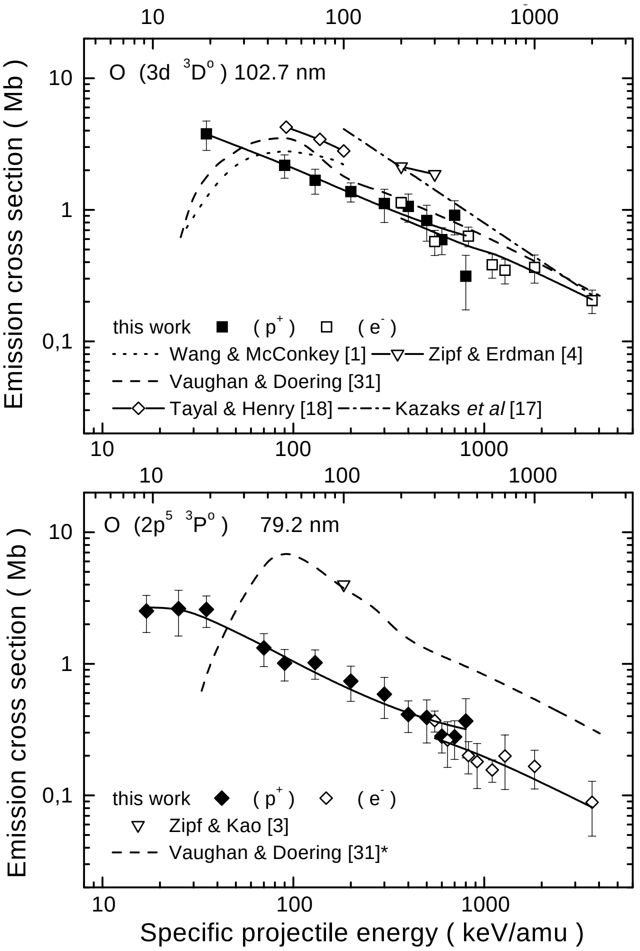

Fig. 10. Emission cross-sections for fluorescence lines resulting from excitation into the O ($3d$ ^{3}D^o) and O ($2p^5$ ^{3}P^o) states by proton impact (compact symbols) and electron impact (open symbols) as function of specific projectile energy (proportional to the square of the projectile velocity). The fitting functions are plotted as line graphs. Error bars include statistical errors only. Our results are compared to published data from various experimental and theoretical investigations. $*$ indicates conversion of excitation cross-sections into emission cross-sections applying the autoionisation factors.

and of 0.110 ± 0.021 for electron impact. Proton and electron impact on O_2 yield a 79.7 nm line to 71.9 nm line branching ratio of 0.099 ± 0.013 and of 0.109 ± 0.021, respectively (paper I, [7]). Theoretical transition probabilities [32] yield a branching ratio of 0.094.

3.2 Emission cross-sections for transitions in O following 2p $\longrightarrow$ 3ℓ and 2s $\longrightarrow$ 2p excitation

Absolute emission cross-sections of fluorescence lines resulting from proton and electron impact excitation of O are displayed in Figures 9 and 10. Partial excitation processes of O have been studied more extensively than partial ionisation processes (see *e.g.* the compilations of Laher and Gilmore [5] and Itikawa and Ichimura [6]). Figures 9 and 10 show our experimental emission cross-sections connected by line graphs from the fitting functions discussed in Section 3.4, along with the previously published cross-sections.

For the excited O (3ℓ) states, only VUV fluorescence lines emitted in transitions into the atomic oxygen O ($2p^4$ ^{3}P^e) ground state were investigated. Branching transitions within the $n = 3$ shell lead to fluorescence in the visible or infrared spectral region. Since the probability for spontaneous fluorescence emission is proportional to the product of the dipole matrix element of the respective transition times the cube of the fluorescence frequency ν^3, the fluorescence lines in the visible should be negligible in intensity with respect to the VUV lines.

3.2.1 The 98.9 nm line emission cross-sections for the transition O ($3s'$ ^{3}D^o) → O ($2p^4$ ^{3}P^e)

The 98.9 nm line emission cross-sections are presented in the upper graph of Figure 9. The excited O ($3s'$ ^{3}D^o) state decays under fluorescence emission only. One possible radiative transition for cascade population of O ($3s'$ ^{3}D^o) inside the wavelength range of the experiment is tabulated at 382.5 nm [12], but is within the wavelength range of the second negative band system of O_2^+ (*cf.* Sect. 2.7.3). Therefore the contribution of cascade decay of higher atomic states to the population of O ($3s'$ ^{3}D^o) cannot be clarified from the recorded spectra. However, Vaughan and Doering [31] assume that cascades contribute 25% or less to the emission cross-section.

Experimental emission and ionisation cross-sections and theoretical ionisation cross-sections are only available for electron impact. Conformity of the presented emission cross-section with the emission cross-section experimentally determined by Wang and McConkey [1] can be seen, even if both experiments do not coincide in exciting electron energies. Summarizing the discussion of experimental results in Laher and Gilmore [5], it is recommended that the experimental emission cross-section of Zipf and Erdmann [4] should be reduced by a factor 2–3. This would lead to agreement with the emission cross-section of this study and with the results of Wang and McConkey. Vaughan and Doering [31] obtained their excitation cross-sections from an electron energy loss experiment (not influenced by cascades). Their results are seen to lie slightly below the present emission cross-section for electron impact, which is not considered as significant with respect to the uncertainties of both experiments. The theoretical excitation cross-sections of Tayal and Henry [18] are not in the electron energy range of the present experiment but are in the same order of magnitude as our emission cross-sections.

3.2.2 The 87.9 nm line emission cross-sections for the transition O ($3s''$ ^{3}P^o) → O ($2p^4$ ^{3}P^e)

The 87.9 nm line emission cross-sections are presented in the bottom graph of Figure 9. The contribution of cascade transitions to the population of O ($3s''$ ^{3}P^o) cannot be tested in the measured spectra, because no cascade transitions inside the wavelength range of fluorescence detection are known to us. The excited state O ($3s''$ ^{3}P^o) autoionises with an autoionisation factor of 0.46 [5]. In order to compare the experimental emission cross-sections with experimental excitation cross-sections, excitation cross-sections have been converted into emission cross-sections by multiplying them with 0.54 according to the autoionisation factor 0.46.

Extrapolation of the electron impact emission cross-sections of Wang and McConkey [1] would lead to suitable harmony with our results. The electron impact emission cross-sections of Zipf and Kao [3] exceed the emission cross-sections of this study as already stated for the 98.9 nm line and 83.3 nm line emission cross-sections. The experimental excitation cross-sections of Vaughan and Doering [31] have been converted into 87.9 nm line emission cross-sections in the way mentioned above. The resulting emission cross-sections in Figure 9 are a factor 2 larger than our emission cross-sections. This cannot be due to cascade population since cascade population would enlarge the optically measured emission cross-sections. The difference of our emission cross-sections to the emission cross-sections deduced from the excitation cross-sections of Vaughan and Doering [31] may be explained by a to small autoionisation factor or by fluorescence emission at 395.4 nm in the O ($3s''$ ^{3}P^o) → O ($3p$ ^{3}P^e) transition. Considering the uncertainties there is at least no contradiction between the cross-sections in Figure 9 (bottom), except the emission cross-sections determined by Zipf and Kao [3].

3.2.3 The 102.7 nm line emission cross-sections for the transition O ($3d$ ^{3}D^o) → O ($2p^4$ ^{3}P^e)

The 102.7 nm line emission cross-sections are illustrated in the upper graph of Figure 10. The excited O ($3d$ ^{3}D^o) state cannot autoionise (*cf.* Fig. 1). One cascade transition into O ($3d$ ^{3}D^o) is specified in the wavelength range of the visible spectra: O ($3p'$ ^{3}D^e) → O ($3d$ ^{3}D^o) at 632.4 nm [12]. In the visible spectrum in Figure 6 (bottom) fluorescence is seen between 625 nm and 640 nm which cannot be unambiguously identified due to the limited resolution.

The 102.7 nm line emission cross-sections for electron impact in Figure 10 seem to meet the emission cross-sections of Wang and McConkey [1], when extrapolated. The experimental O ($3d$ ^{3}D^o) excitation cross-section of Vaughan and Doering [31] are in good accord with our results. The emission cross-sections of Zipf and Erdman [4], the theoretical O ($3d$ ^{3}D^o) excitation cross-sections of Kazaks *et al.* [17], (approaching our emission cross-sections at high electron energies) and Tayal and Henry [18] (no matching electron energies with our experiment) exceed our electron impact emission cross-sections in the mean by a factor 2. Agreement of all emission and excitation cross-sections can be stated with respect to the reported uncertainties. From the agreement of emission and excitation cross-sections we conclude that cascade population of O ($3d$ ^{3}D^o) is negligible within the experimental uncertainties.

3.2.4 The 79.2 nm line emission cross-sections for the transition O ($2p^5$ ^{3}P^o) → O ($2p^4$ ^{3}P^e)

The 79.2 nm line emission cross-sections are shown in the bottom graph of Figure 10. The 79.2 nm fluorescence line results from $2s \rightarrow 2p$ excitation which is only observable in open shell atoms. In the atomic spectrum in Figure 4 (bottom graph) it is obvious that fluorescence at 79.2 nm is not clearly separated from fluorescence at 79.7 nm emitted by O^+ ($2s^{-1}$ ^{2}D^e). A fitting routine had to be applied in order to get the fluorescence intensity at 79.2 nm.

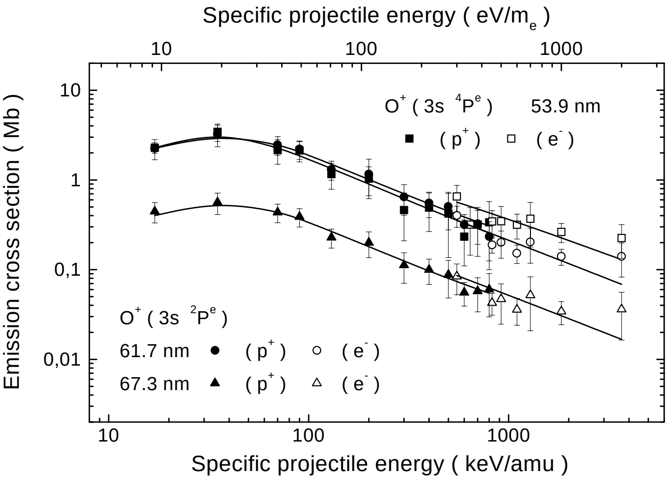

Fig. 11. Emission cross-sections for fluorescence lines resulting from ion excitation into the O$^+$ ($3s$ ^{4}P^e) and O$^+$ ($3s$ ^{2}P^e) states by proton impact (compact symbols) and electron impact (open symbols) as function of specific projectile energy (proportional to the square of the projectile velocity). The fitting functions are plotted as line graphs. Error bars include statistical errors only.

The transition O ($2p^5$ ^{3}P^o) → O ($2p^4$ ^{3}P^e) is listed as the only radiative transition of the excited O ($2p^5$ ^{3}P^o) state [12], but O ($2p^5$ ^{3}P^o) autoionises with an autoionisation factor 0.51 [5]. No cascade transitions that populate O ($2p^5$ ^{3}P^o) from higher excited atomic states have been found. They could only result from the excitation of a $2s$-electron into a higher excited state and should be rather weak due to strong autoionisation of the cascading level.

In order to compare the 79.2 nm line emission cross-sections to the experimental O ($2p^5$ ^{3}P^o) excitation cross-sections of Vaughan and Doering [31], the excitation cross-sections have been converted into emission cross-sections by multiplication with 0.49, according to the autoionisation factor 0.51. The converted excitation cross-sections are seen to agree with the value of Zipf and Kao [3] then. Both cross-sections are a factor 4 larger than the emission cross-sections determined in this work. We remember that the 87.9 nm line emission cross-section of Zipf and Kao [3] overestimated our 87.9 nm line emission cross-section as well as the converted excitation cross-section of Vaughan and Doering [31].

3.3 Emission cross-sections for transitions in O$^+$ following O$^+$ (3s ^{4}P^e) and O$^+$ (3s ^{2}P^e) ion excitation

The 53.9 nm line emission cross-section (O$^+$ ($3s$ ^{4}P^e) → O^+ ($2p^3$ ^{4}S^o)) and the 61.7 nm line/67.3 nm line emission cross-section (O$^+$ ($3s$ ^{2}P^e) → O$^+$ ($2p^3$ ^{2}D^o / ^{2}P^o)) for proton and electron impact are presented in Figure 11. In contrast to our results for dissociative ionisation of O$_2$ by proton and electron impact in paper I [7] and for photoionisation of O [8], fluorescence intensity at 53.8 nm/53.9 nm cannot be attributed to the 53.9 nm line resulting from O$^+$ ($3s$ ^{4}P^e) ion excitation only. This becomes apparent when the intensity ratio of the fluorescence lines at 53.8 nm/53.9 nm and at 58.1 nm in the atomic spectrum in Figure 4 is compared with the molecular spectrum. Multiplying the intensity at 58.1 nm with the 53.8 nm line to 58.1 nm line branching ratio 4.0 [14], the resulting intensity at 53.8 nm gives a minor contribution to the fluorescence intensity at 53.9 nm for dissociative ionisation in the molecular spectrum but similar intensities at 53.8 nm and 53.9 nm in the atomic spectrum.

The mean branching ratio for 67.3 nm to 61.7 nm fluorescence emission in the VUV spectra for proton impact of 0.178 ± 0.023 and for electron impact of 0.243 ± 0.046 is in good accord with the experimental values of 0.19 from our photoionisation experiment [8], of 0.182 ± 0.024 for proton impact on O$_2$ and of 0.232 ± 0.050 for electron impact on O$_2$ (paper I [7]) and finally also with the theoretical branching ratio of 0.16 derived from transition probabilities calculated by Bell *et al.* [32].

For the O$^+$ ($3s$ ^{4}P^e) and O$^+$ ($3s$ ^{2}P^e) states, cascade population is observed in the visible spectrum in Figure 6. Four emission multiplets with relative strong fluorescence intensity, assigned in the bottom graph of Figure 6, namely O$^+$ ($3p$ ^{2}P^o) → O$^+$ ($3s$ ^{2}P^e) at 392.0–398.3 nm, O$^+$ ($3p$ ^{4}P^o) → O$^+$ ($3s$ ^{4}P^e) at 431.7–436.7 nm, O$^+$ ($3p$ ^{2}D^o) → O$^+$ ($3s$ ^{2}P^e) at 441.5–445.2 nm and O$^+$ ($3p$ ^{4}D^o) → O$^+$ ($3s$ ^{4}P^e) at 463.9–467.6 nm are recognized to feed the O$^+$ ($3s$ ^{4}P^e) and the O$^+$ ($3s$ ^{2}P^e) state. The identification of the transitions has been carried out according to the high resolution spectrum measured for electron impact on O$_2$ in paper I [7]. The observed cascade transitions result from ionisation of a $2p$-electron and simultaneous excitation of a second $2p$-electron into a $3p$-state. The O$^+$ ($3p$) excited ion states can only decay into the O$^+$ ($3s$ ^{4}P^e) and O$^+$ ($3s$ ^{2}P^e) states. Although no emission cross-sections could be determined in the visible spectral range, the two-electron processes of O$^+$ ($3s$) and O$^+$ ($3p$) ion excitation can be expected to have cross-sections in the same order of magnitude.

3.4 Bethe-Fano plots of the emission cross-sections

The Bethe-theory [30] can be applied to fast collisions. In the present experiment the asymptotic Bethe-formulae are expected to reproduce the experimental emission cross-sections qualitatively for the high electron velocities. The asymptotic Bethe-formulae have therefore been parametrized for the use as fitting functions for the electron impact emission cross-sections:

$$\sigma = \frac{a}{E}\ln(bE) \quad \text{for optically allowed transitions} \tag{7}$$

$$\sigma = \frac{c}{E} \quad \text{for optically forbidden transitions.} \tag{8}$$

Since the Bethe-theory cannot be applied to describe the whole proton velocity range covered in our experiment, an inverse polynomial fitting function has been used for the proton impact emission cross-sections

$$\sigma = a_0 + \frac{a_1}{x - x_0} + \frac{a_2}{(x - x_0)^2}\,. \tag{9}$$

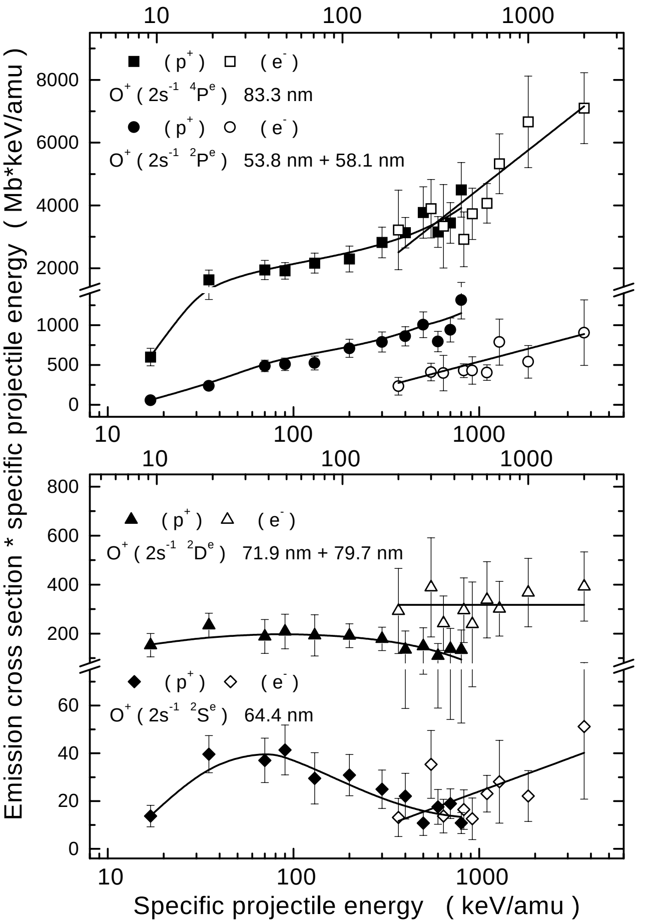

Fig. 12. Bethe-Fano plots of emission cross-sections for fluorescence lines resulting from $2s^{-1}$ ionisation by proton impact (compact symbols) and electron impact (open symbols). The fitting functions are plotted as line graphs. Error bars include statistical errors only. Emission cross-sections of fluorescence lines originating from the same O^+ $(2s^{-1})$ state are summed.

At equivalent and sufficiently high projectile velocities the Bethe-theory predicts equal ionisation cross-sections for electron and proton impact. Such a behaviour is observed for all presented emission cross-sections within the experimental uncertainties, most striking for the most intensive fluorescence emission at 83.3 nm.

Bethe-Fano plots display the products of emission cross-section times specific projectile energy *versus* the logarithm of specific projectile energy (Figs. 12–14). The Bethe-Fano plots for emission cross-sections resulting from the same excited ionic state are summed to outline the characteristics of the ionisation and excitation processes.

A principal difference in the $2s^{-1}$ ionisation into the final ionic states O^+ $(2s^{-1}\ {}^4P^e)$ and O^+ $(2s^{-1}\ {}^2P^e)$ on the one hand and O^+ $(2s^{-1}\ {}^2D^e)$ and O^+ $(2s^{-1}\ {}^2S^e)$ on the other can be seen in Figure 12. The linear increase in the Bethe-Fano plots of the emission cross-sections resulting from $2s^{-1}$ ionisation into O^+ $(2s^{-1}\ {}^4P^e)$ and O^+ $(2s^{-1}\ {}^2P^e)$ indicates ionisation *via* an optically allowed transition according to the asymptotic Bethe-formula in equation (7). In contrast the Bethe-Fano connected to $2s^{-1}$ ionisation into O^+ $(2s^{-1}\ {}^2D^e)$ tends to a constant behaviour indicating an optically forbidden transition. The Bethe-Fano plot for $2s^{-1}$ ionisation into O^+ $(2s^{-1}\ {}^2S^e)$ for electron impact seems to increase with electron energy. Due to scatter in the electron impact emission cross-sections, a constant would fit the data also. Though the Bethe-theory is not applicable to our proton impact data, a Bethe-Fano plot is appropriate to underline the dependence of the cross-sections on the projectile energy. For proton impact a maximum appears in the Bethe-Fano plot. Similar Bethe-Fano plots have been obtained by our workgroup in the investigation of Ne double ionisation by proton and electron impact [28], interpreted as a hint for successive collisions of the projectile with two target electrons or a collision of the first ejected electron with a second bound electron. Finally, we note that all four partial $2s^{-1}$ photoionisation channels were observed in our photoionisation experiment [8], in contrast to the possible classification of O^+ $(2s^{-1}\ {}^2D^e)$ and O^+ $(2s^{-1}\ {}^2S^e)$ ionisation as optically forbidden in the independent particle model and as a manifestation of electron correlations.

Bethe-Fano plots of the emission cross-sections for the excitation processes discussed above are presented in Figure 13. The linear increase of the products of emission cross-section and specific projectile energy with the logarithm of the specific projectile energy characterizes the excitations as optically allowed. The asymptotic Bethe-formula for excitation cross-sections [30] links the slope of a Bethe-Fano plot with the optical oscillator strength of the respective transition. From the fitting parameters, the optical oscillator strengths of the investigated excitations have been determined. They are compared with optical oscillator strengths from an electron energy loss experiment by Doering *et al.* [33] and with theoretical optical oscillator strengths calculated by Pradhan and Saraph [34] and by Tayal and Henry [18] in Table 2. The optical oscillator strengths derived from our emission cross-sections agree well with the other results for the O (3ℓ) states, but underrate the published optical oscillator strengths in case of the O $(2p^5\ {}^3P^o)$ excited states.

Figure 14 shows Bethe-Fano plots of the emission cross-sections of the 53.9 nm line and 61.7 nm line plus 67.3 nm line. The rise of the Bethe-Fano plots for electron impact with increasing electron energy suggests that population of the O^+ $(3s\ {}^4P^e)$ and O^+ $(3s\ {}^2P^e)$ excited ion states takes place *via* optically allowed transitions in fast collisions. This is in contradiction to the expectation from the independent particle model which treats ion excitation as a two electron process. We interpret the observed high velocity behaviour as resulting from atomic ground state configuration interaction (ISCI) allowing a one electron ionisation process. The strong appearance of the discussed ionic states in our photoionisation experiment [8] supports the above interpretation. So Figure 14 demonstrates an interesting transition from a two step process at the lower proton velocities to a sudden transition described by configuration interaction [35].

Table 2. Optical oscillator strengths obtained from the Bethe-Fano plots in Figure 13, experimentally determined by Doering *et al.* [33] and theoretically calculated by Pradhan and Saraph [34] and Tayal and Henry [18].

Excitation & Fluorescence wavelength	Optical oscillator strength			
	this work	Doering *et al.*	Pradhan & Saraph	Tayal & Henry[2]
O ($2p^4\,{}^3P^e$) → O ($3d\,{}^3D^o$) 102.7 nm	0.021	0.019	0.0203	0.030 (l) 0.023 (v)
O ($2p^4\,{}^3P^e$) → O ($3s'\,{}^3D^o$) 98.9 nm	0.071	0.061	0.0558	0.060 (l) 0.051 (v)
O ($2p^4\,{}^3P^e$) → O ($3s''\,{}^3P^o$) 87.9 nm [1]	0.077	0.086	0.0791	–
O ($2p^4\,{}^3P^e$) → O ($2p^5\,{}^3P^o$) 79.2 nm [1]	0.025	0.070	0.0695	–

[1] Autoionising excited state, [2] (l) length form (v) velocity form.

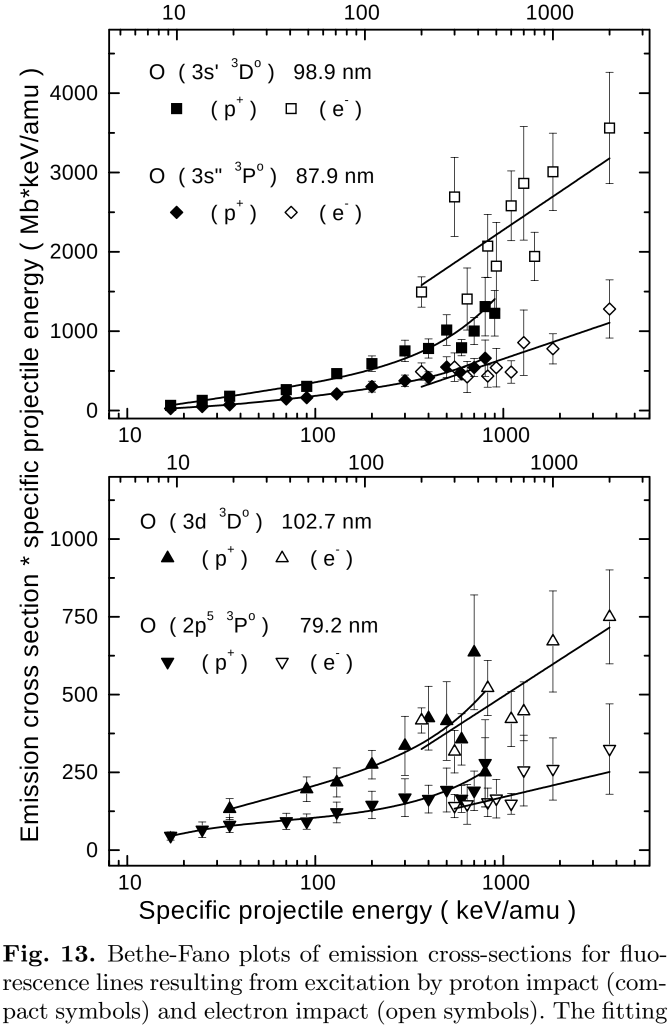

Fig. 13. Bethe-Fano plots of emission cross-sections for fluorescence lines resulting from excitation by proton impact (compact symbols) and electron impact (open symbols). The fitting functions are plotted as line graphs. Error bars include statistical errors only.

4 Summary

We have presented a comprehensive study of absolute emission cross-sections of VUV fluorescence lines emitted from excited O$^+$ and O states after electron and proton impact on O. In combination with the investigation of fluorescence resulting from proton and electron impact on O$_2$ in paper I [7], from photoionisation of O [8] and from photodissociation of O$_2$ [9], the presented results provide extensive data for fluorescence spectroscopic applications concerning oxygen.

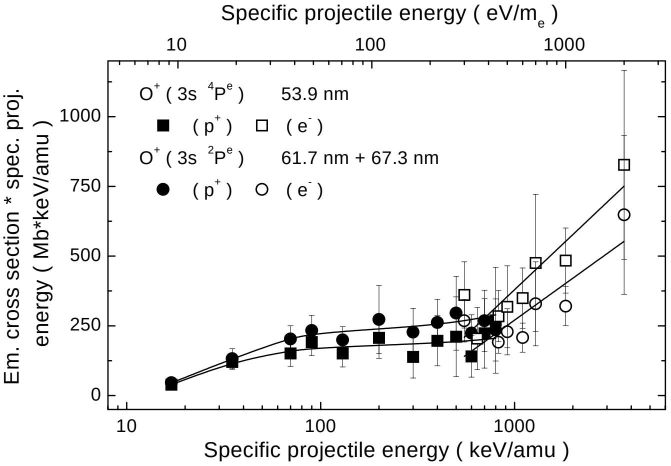

Fig. 14. Bethe-Fano plots of emission cross-sections for fluorescence lines resulting from ion excitation by proton impact (compact symbols) and electron impact (open symbols). The fitting functions are plotted as line graphs. Error bars include statistical errors only. The emission cross-sections of fluorescence lines originating from the O$^+$ ($3s\,{}^2P^e$) state are summed.

The electron impact emission cross-sections assigned to atomic excitation processes are in suitable harmony with the so far published experimental emission cross-sections. Agreement with experimental (electron energy loss) and theoretical excitation cross-sections is seen in case of the non-autoionising excited O states. The deviation in case of autoionising excited O states questions the employed autoionisation factors. For proton impact neither partial excitation cross-sections nor emission cross-sections have been available for comparison.

Four partial $2s^{-1}$ ionisation channels are observed. Ionisation into the O$^+$ ($2s^{-1}\,{}^2D^e$) state and the O$^+$ ($2s^{-1}\,{}^2S^e$) state are investigated for the first time. An interpretation based on Bethe-Fano plots points out a difference in the $2s^{-1}$ ionisation mechanism populating the O^+ ($2s^{-1}$ $^2D^e$) and O^+ ($2s^{-1}$ $^2S^e$) states on the one hand and the O^+ ($2s^{-1}$ $^4P^e$) and O^+ ($2s^{-1}$ $^2P^e$) states on the other. The latter ionisation channels can be explained by a simple one electron ejection whereas the former need either to be considered as two electron processes in the independent particle model or require configuration interaction wavefunctions to describe the atomic ground state or the $2s^{-1}$ ion states. The importance of electron correlations is also implied by the Bethe-Fano plots for ion excitation into the O^+ ($3s$ $^4P^e$) state and the O^+ ($3s$ $^2P^e$) state.

This work was financially supported by the Deutsche Forschungsgemeinschaft DFG. The help of A. Werner in the preparation of the experiment is gratefully acknowledged. Thanks to G. Trylat for supporting the experimental setup and operating the accelerator.

References

1. S. Wang, J.W. McConkey, J. Phys. B: At. Mol. Opt. Phys. **25**, 5461 (1992).
2. E.C. Zipf, W.W. Kao, R.W. McLaughlin, Chem. Phys. Lett. **118**, 591 (1985) for electron energies $\leq$ 300 eV; E.C. Zipf, W.W. Kao, P.W. Erdmann, cited in Laher and Gilmore [5] for electron energies $\geq$ 300 eV.
3. E.C. Zipf, W.W. Kao, Chem. Phys. Lett. **125**, 394 (1986).
4. E.C. Zipf, P.W. Erdmann, cited in Laher and Gilmore [5] and Itikawa and Ichimura [6].
5. R.R. Laher, F.R. Gilmore, J. Phys. Chem. Ref. Data **19**, 277 (1990).
6. Y. Itikawa, A. Ichimura, J. Phys. Chem. Ref. Data **19**, 637 (1990).
7. O. Wilhelmi, K.-H. Schartner, Eur. Phys. J. D **11**, 79 (2000).
8. O. Wilhelmi, G. Mentzel, B. Zimmermann, K.-H. Schartner, H. Liebel, H. Schmoranzer, B.M. McLaughlin, Phys. Rev. A **60**, 3702 (1999).
9. H. Liebel, S. Lauer, F. Vollweiler, R. Müller-Albrecht, A. Ehresmann, H. Schmoranzer, G. Mentzel, K.-H. Schartner, O. Wilhelmi, Phys. Lett. A (submitted, 1999).
10. W. Jans, B. Möbus, M. Kühne, G. Ulm, A. Werner, K.-H. Schartner, Phys. Rev. A **55**, 1890 (1997).
11. R.L. Kelly, J. Phys. Chem. Ref. Data **16** (Suppl. 1), 85 (1987).
12. A.R. Striganov, N.S. Sventitskii, *Tables of spectral lines of neutral and ionised atoms* (IFI/Plenum, New York – Washington, 1968).
13. P.H. Krupenie, J. Phys. Chem. Ref. Data **1**, 423 (1972).
14. H.J. Flaig, K.-H. Schartner, E. Träbert, P.H. Heckmann, Phys. Scripta **31**, 255 (1985).
15. G. Peach, J. Phys. B: At. Mol. Opt. Phys. **3**, 328 (1970); J. Phys. B: At. Mol. Opt. Phys. **4**, 1670 (1971).
16. S. Chung, C.C. Lin, E.T.P. Lee, Phys. Rev. A **47**, 3867 (1993).
17. P.A. Kazaks, P.S. Ganas, A.E.S. Green, Phys. Rev. A **6**, 2169 (1972)
18. S.S. Tayal, R.J.W. Henry, Phys. Rev. A **39**, 4531 (1989).
19. S.J. Schaphorst, M.O. Krause, C.D. Caldwell, H.P. Saha, M. Pahler, J. Jiménez-Mier, Phys. Rev. A **52**, 4656 (1995).
20. J.A.R. Samson, V.E. Petrosky, Phys. Rev. A **9**, 2449 (1974).
21. W.C. Stolte, Y. Lu, J.A.R. Samson, O. Hemmers, D.L. Hansen, S.B. Whitfield, H. Wang, P. Glans, D.W. Lindle, J. Phys. B: At. Mol. Opt. Phys. **30**, 4489 (1997).
22. J.A.R. Samson, P.N. Pareek, Phys. Rev. A **31**, 1470 (1985).
23. F.J. Comes, F. Speier, A. Elzer, Z. Naturforsch. **23a**, 125 (1968).
24. P.B. Cairns, J.A.R. Samson, Phys. Rev. A **139**, 1403 (1965).
25. P. van der Meulen, C.A. de Lange, M.O. Krause, D.C. Mancini, Phys. Scripta **41**, 837 (1990).
26. H. Pauly, in *Atomic and molecular beam methods*, edited by G. Scales (Oxford University Press, 1988).
27. A. Werner, Ph.D. thesis, Justus-Liebig-Universität Giessen, 1997.
28. M. Eckhardt, K.-H. Schartner, Z. Phys. A **312**, 321 (1983).
29. R. Hippler, K.-H. Schartner, J. Phys. B: At. Mol. Opt. Phys. **7**, 1167 (1974), Ar 3s-electron ionisation cross-sections multiplied with 1.3 (private communication).
30. M. Inokuti, Rev. Mod. Phys. **43**, 297 (1971).
31. S.O. Vaughan, J.P. Doering, cited in Laher and Gilmore [5] and Itikawa and Ichimura [6].
32. K.L. Bell, A. Hibbert, R.P. Stafford, B.M. McLaughlin, Phys. Scripta **50**, 343 (1994).
33. J.P. Doering, E.E. Gulcicek, S.O. Vaughan, J. Geophys. Res. **90**, 5279 (1985).
34. A.K. Pradhan, H.E. Saraph, J. Phys. B: At. Mol. Opt. Phys. **10**, 3365 (1977).
35. K.-H. Schartner, B. Lommel, D. Detleffsen, J. Phys. B: At. Mol. Opt. Phys. **24**, L13 (1991).